

See discussions, stats, and author profiles for this publication at: <https://www.researchgate.net/publication/231396455>

# Structural and Catalytic Properties of Model Supported Nickel Catalysts

ARTICLE *in* THE JOURNAL OF PHYSICAL CHEMISTRY · JANUARY 1994

Impact Factor: 2.78 · DOI: 10.1021/j100055a033

---

CITATIONS

42

---

READS

9

## 3 AUTHORS, INCLUDING:



Kent E. Coulter

Southwest Research Institute

34 PUBLICATIONS 662 CITATIONS

SEE PROFILE



Xueping Xu

II-VI Incorporated

64 PUBLICATIONS 1,906 CITATIONS

SEE PROFILE

# Structural and Catalytic Properties of Model Supported Nickel Catalysts

Kent Coulter, Xueping Xu, and D. Wayne Goodman\*

Department of Chemistry, Texas A&M University, College Station, Texas 77843-3255

Received: August 18, 1993; In Final Form: November 19, 1993\*

The surface structure and catalytic properties of model silica-supported nickel catalysts have been investigated with infrared reflection-absorption spectroscopy (IRAS) and reaction kinetics of ethane hydrogenolysis and carbon monoxide methanation. Nickel particles in the range 15–80 Å were vacuum deposited onto silica thin films using established preparation procedures. Specific rates and activation energies for ethane hydrogenolysis and carbon monoxide methanation over the model catalysts are remarkably similar to the corresponding values for both traditional silica-supported nickel catalysts and nickel single crystals. The turnover frequency for CO methanation is independent of particle size for the dimensions studied. The ethane hydrolysis rate, however, increases with particle size to a maximum at ~25 Å and then decreases. This reactivity trend is found to parallel a change in the percentage of bridging CO on the nickel particles as determined by IRAS.

## Introduction

An understanding of the relationship among surface structure, particle size, and chemical properties is of primary importance in the design of a catalyst.<sup>1</sup> Typically, oriented single crystals have been used as model catalysts to investigate the influence of morphology on reactivity/selectivity. These surface science studies, under well-defined conditions, have provided insights into the catalytic mechanisms, active sites, and reacting species of heterogeneous catalysts at the molecular level.<sup>2</sup> There are, however, distinct differences between the well-defined single crystals used in surface science studies and metal catalysts supported on high surface area oxides. It has been shown that the interaction between a dispersed model catalyst and its support can modify the activity of the catalyst depending on the reaction and the reaction conditions.<sup>3</sup> These metal-support interactions have been investigated by depositing an oxide onto the surface of a single-crystal metal surface and monitoring the modifications to the reactivity of the metal.<sup>4</sup> There are inherent problems with this approach to studying supported metal catalysts in that the metal maintains its bulklike characteristics. This is contrary to the effects observed for dispersed metal catalysts, where activity and selectivity often depend upon the size of the metal particle.<sup>5</sup>

A more favorable approach to the synthesis of a realistic model of a dispersed supported metal catalyst is to deposit a metal onto an oxide support material. The incorporation of surface science techniques in the study of these model supported metal catalysts has been limited due to the experimental difficulties related to sample mounting, sample heating/cooling, and surface charging of insulating oxides. Recently, we have circumvented these problems with an approach utilizing metal deposition onto a silicon dioxide thin film (~100 Å) which, in turn, is supported on a molybdenum metal substrate.<sup>6–8</sup> These planar SiO<sub>2</sub> thin film models have been shown to be good models for high surface area silica.<sup>9</sup> The Mo(110) substrate does not alter the chemical properties of the thin film, yet improves the thermal stability of the SiO<sub>2</sub> relative to SiO<sub>2</sub> grown on silicon.<sup>9,10</sup>

The specific activity of supported nickel catalysts toward alkane hydrogenolysis generally depends markedly upon the metal particle size.<sup>5,11</sup> Specific activity is defined as the catalytic rate normalized to the number of exposed metal atoms and is therefore representative of the molecules produced per surface atom. Although the relationship between particle size and activity has been well documented, there is not a generally accepted expla-

nation at present. Martin<sup>12</sup> and Goodman<sup>13</sup> have suggested that the activity of different crystal planes toward hydrogenolysis is responsible for the observed variations in activity with metal particle size. Single-crystal surface science studies have shown these structure-sensitive reactions to proceed more rapidly over the (100) crystal plane compared to the (111) facet.<sup>13</sup> A direct experimental verification of the single-crystal results using supported metal catalysts has not been made due to the difficulties encountered with oxide support materials in surface science studies and the inability to characterize the precise morphology of small metal clusters with traditional catalyst characterization techniques.<sup>14</sup>

In contrast to alkane hydrogenolysis, carbon monoxide methanation is structure insensitive and exhibits little variation in specific activity with change in particle size.<sup>11</sup> The close correspondence of specific activity, pressure effects, and apparent activation energies among studies over high surface area supported nickel,<sup>15,16</sup> nickel single crystals,<sup>11,17–19</sup> and nickel supported on model thin-film alumina<sup>20</sup> is evidence of the structure insensitivity of the methanation reaction. Single-crystal kinetic studies have shown the mechanism of methanation to involve dissociation of CO and the subsequent hydrogenation of the resulting carbon species. The active surface carbon species is a carbidic type which is generally formed for all methanation catalysts.<sup>17</sup> The removal rate of carbon by hydrogen is in delicate balance with the formation of surface carbide.

In this paper, we investigated the structural and kinetic properties of model silica-supported nickel catalysts which are used for alkane hydrogenolysis and CO methanation. Metal particle size and kinetic properties have been studied using a combination of ultrahigh-vacuum (UHV) surface science techniques and elevated pressure kinetic measurements. The results are compared with measurements from traditional supported nickel catalysts and nickel single crystals.

## Experimental Section

The experiments were carried out in two UHV surface analysis chambers. One chamber is equipped with Auger electron spectroscopy (AES), quadrupole mass spectrometry (QMS), gas and metal dosing capabilities, and a Mattson Cygnus 100 FTIR spectrometer for IR single reflection-absorption spectroscopy (IRAS) studies. The details of the apparatus have been described elsewhere.<sup>21</sup> The IRAS spectra were acquired at an incident angle of 85° and were averages of 128 scans at 4-cm<sup>-1</sup> resolution. All spectra were taken at a base pressure of less than 10<sup>-9</sup> Torr.

\* Abstract published in *Advance ACS Abstracts*, January 1, 1994.

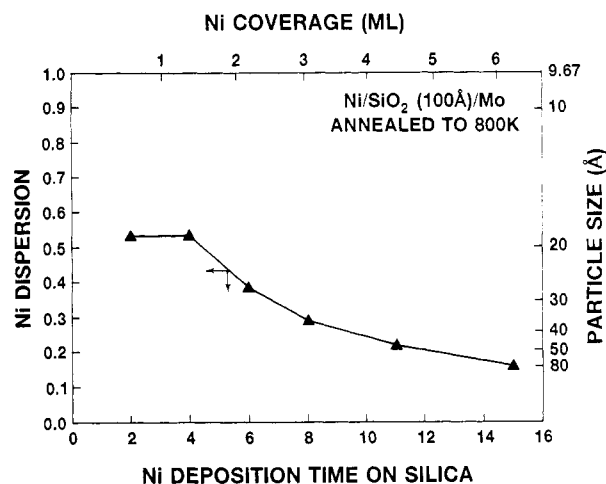


**Figure 1.** Nickel dispersion and particle size as a function of deposition time for nickel evaporated onto a thin film ( $\sim 100$  Å) of silica. The nickel deposition was at room temperature followed by an anneal to 800 K.

The second chamber is a combined UHV/reactor cell system that allows sample transfer from UHV conditions to a reaction cell for kinetic studies at pressures up to 1000 Torr. The UHV portion of the second chamber is equipped with AES, QMS, and dosing capabilities for both gases and metals.

The preparation and characterization of the silica thin films on Mo(110) have been previously reported.<sup>8,22,23</sup> Nickel was evaporated onto the silica thin film ( $\sim 100$  Å) at room temperature and annealed to 800 K. The nickel coverage, dispersion, and structure were determined with temperature-programmed desorption (TPD), IRAS of CO, and AES.<sup>24</sup> The nickel flux was monitored with line-of-site QMS during evaporation.

In the kinetic studies, following preparation and characterization of the sample in the UHV chamber, the model catalyst was transferred in situ to the reaction cell via a double-stage differentially pumped sliding Teflon seal.<sup>21</sup> Ethane hydrogenolysis experiments were run in 1.0 Torr of triply-distilled  $C_2H_6$  and 20.0 Torr of  $H_2$  over the temperature range 500–650 K. Carbon monoxide methanation experiments were run in 5.0 Torr of CO and 20.0 Torr of  $H_2$  over the temperature range 570–625 K. In both reactions, the reactants were allowed to mix in the reactor for 5 min and the subsequent experiment run for 10 min. Following reaction, the product gas mixture was analyzed with gas chromatography (GC) utilizing a flame ionization detector.

## Results

**Nickel Particle Characterization.** Figure 1 shows the dispersion of nickel as a function of nickel deposition for nickel films deposited at room temperature and annealed to 800 K. Dispersion, defined as the ratio of exposed surface atoms to total metal atoms, was measured using TPD.<sup>7</sup> The total amount of nickel was determined by Ni desorption from the silica film and calibrated using the corresponding TPD peak area from 1 monolayer (ML) of nickel on Mo(110).<sup>25</sup> The nickel surface area was obtained using CO TPD, assuming the saturation coverage of CO on Ni at 300 K to be  $\sim 0.5$  ML.<sup>26–28</sup> CO TPD of saturation CO/Mo(110) ( $\theta_{CO} = 0.5$  ML) was used as a reference for the nickel CO TPD area. The average particle size was estimated from dispersion assuming spherical particles and verified with atomic force microscopy, which showed particles in the range predicted by the TPD dispersion measurements.<sup>29</sup>

The nickel was annealed to 800 K to promote 3D clustering of the nickel particles.<sup>7</sup> Annealing decreased the nickel surface area by a factor of 2 and also stabilized the surface structure. The highest dispersion, at a nickel coverage of  $\sim 0.6$  ML, corresponds to an average particle size of  $\sim 15$  Å. The particle size increased

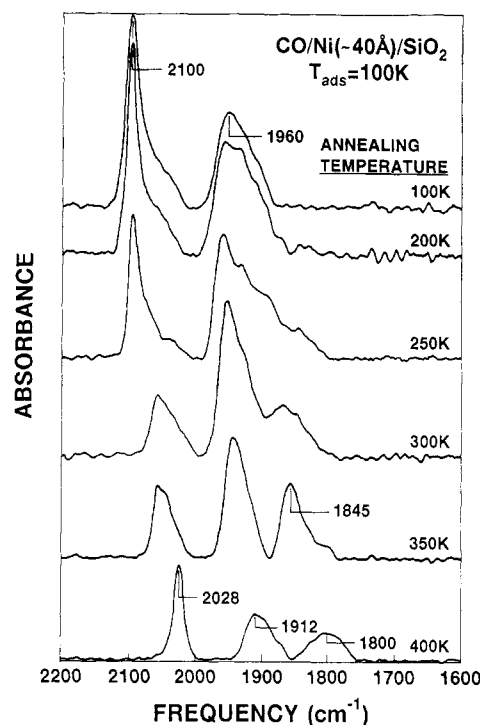


**Figure 2.** IRAS spectra for CO adsorbed onto a model Ni ( $\sim 40$  Å)/SiO<sub>2</sub> catalyst as a function of temperature. CO was adsorbed while cooling from 300 to 100 K, followed by a brief anneal to the indicated temperature.

with deposition time (coverage), yielding 80-Å particles for a nickel coverage of 15 ML.

The surface structure of the nickel particles was investigated using IRAS of adsorbed carbon monoxide. The IRAS spectra for CO on nickel single crystals have been well documented. On low index (111) and (100) nickel surfaces, three CO vibrational features are observed at 2020–2100, 1910–1960, and 1800–1850  $cm^{-1}$ . These bands are assigned to CO adsorption at atop,<sup>27,30,31</sup> twofold,<sup>27,31</sup> and threefold<sup>27,31,32</sup> bridging sites. On Ni(111), CO adsorbs onto bridging sites (both twofold and threefold sites) at low coverages with the observed frequencies shifting from 1823 to 1926  $cm^{-1}$  (twofold sites) as the CO coverage increases. At 300 K, CO at saturation coverage (0.5 ML) on Ni(111) adsorbs exclusively onto twofold bridging sites, forming a  $c(4 \times 2)$  overlayer and exhibiting a frequency of 1908  $cm^{-1}$ . Cooling the Ni(111) surface increases the saturation CO coverage to 0.57 ML, yielding bridging CO at 1926  $cm^{-1}$  and atop CO at 2057  $cm^{-1}$ .<sup>33,34</sup>

At 300 K, saturation CO (0.5 ML) forms a  $c(2 \times 2)$  overlayer on Ni(100) with an atop band at 2048  $cm^{-1}$  and a bridging band at 1949  $cm^{-1}$ . A compressed CO overlayer forms at low temperatures ( $< 250$  K) and high CO coverage, exhibiting bridging CO at 1968  $cm^{-1}$  and atop CO in a broad range from 2035 to 2091  $cm^{-1}$ . The frequencies of both the atop and bridging CO bands on Ni(100) decrease with decreasing CO coverage to 2022 and 1896  $cm^{-1}$  respectively, in the low-coverage limit.<sup>35</sup>

The IRAS spectra of CO adsorbed onto a silica-supported ( $\sim 40$  Å) nickel catalyst as a function of temperature are shown in Figure 2. CO was adsorbed while cooling the sample from 300 to 100 K to ensure a saturation coverage. The spectra were acquired at 100 K after briefly annealing the sample in vacuum to the indicated temperature. At low annealing temperatures ( $< 250$  K), the adsorption bands indicate that CO forms a compressed overlayer on the nickel surface, with CO adsorbing only at atop and twofold bridging sites. Unfortunately, for the compressed overlayer, the effect of crystal orientation on CO adsorption is minimal as evidenced by the IRAS spectra. The 2100- $cm^{-1}$  band is typical of atop CO adsorption in a compressed CO overlayer,<sup>29</sup> whereas the bridge-bound band at 1960  $cm^{-1}$

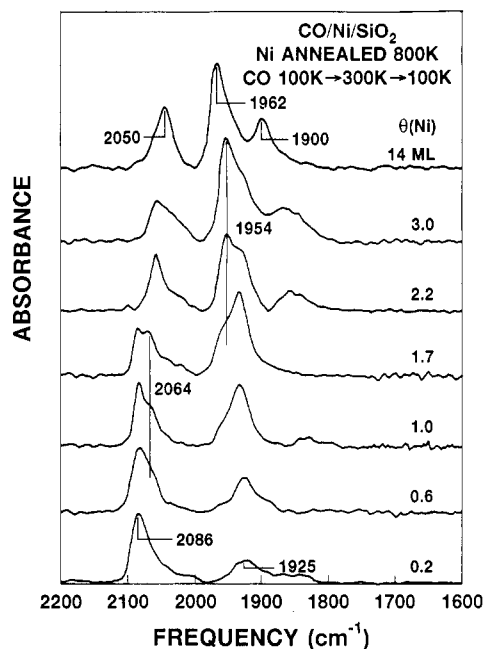


Figure 3. IRAS spectra of CO annealed to 300 K for increasing nickel coverage.

does not correspond to a unique nickel surface structure. Therefore, IRAS spectra of CO adsorbed onto Ni/silica at  $T < 250$  K provide little information with respect to the surface structure of the nickel particles.

Annealing the sample to  $\geq 300$  K relaxes the compressed CO overlayer due to desorption of small amounts of CO. In this temperature range ( $> 300$  K), the IRAS spectrum of CO can be related to the structural features of the nickel particles. In order to gain insight into the surface structure of the nickel particles, the IRAS spectra of different nickel particle sizes at various temperatures are compared to spectra reported for single crystals.

In Figure 3, a series of IRAS spectra are shown for a saturation CO coverage on Ni/SiO<sub>2</sub> after a brief anneal to 300 K. At a very low effective nickel coverage (0.2 ML), two CO IR absorption bands are observed at 2086 and 1925 cm<sup>-1</sup>. As the nickel coverage increases, the intensity of the low-frequency band gradually increases and shifts to 1934 cm<sup>-1</sup>, whereas the intensity of the 2086-cm<sup>-1</sup> band decreases. Additional bands appear as the nickel coverage is increased. A shoulder at 2064 cm<sup>-1</sup> is apparent on the 2086-cm<sup>-1</sup> peak, which, above  $\sim 1.7$  ML, becomes the prevalent high-frequency band. A second new feature at 1954 cm<sup>-1</sup> increases in intensity with an increase in the nickel coverage and becomes the dominant feature in the spectrum for large particles. At  $\sim 2$  ML, a peak at 1856 cm<sup>-1</sup> increases in intensity and shifts to 1900 cm<sup>-1</sup> as the particle size increases. Under the same conditions (300 K), CO exclusively adsorbs onto twofold bridging sites of Ni(111) with a stretching frequency of 1900 cm<sup>-1</sup>. On Ni(100), CO exhibits stretching frequencies of 2050 and 1950 cm<sup>-1</sup> for atop and bridging sites, respectively, with an intensity ratio of 2:1.<sup>30</sup> Correlations between the IRAS spectra of CO on the model catalysts and the reported single-crystal data indicate that large Ni particles ( $> 3$  ML) contain (100) and (111) facets (2050 and 1900 cm<sup>-1</sup>) and additional adsorption sites that favor bridged bound CO adsorption (1960 cm<sup>-1</sup>). The smaller particles, which have a major CO band at 2086 cm<sup>-1</sup>, do not exhibit frequencies characteristic of distinct facets.

**Ethane Hydrogenolysis.** Ethane hydrogenolysis reactions were carried out in order to correlate the observed surface structural changes with catalytic activity. Ethane hydrogenolysis is a classic reaction that has been used to illustrate the effects of structure on catalytic activity.<sup>5</sup> Figure 4 shows the specific reaction rate [(product molecules)·(surface atom)<sup>-1</sup>·(second)<sup>-1</sup>] or turnover frequency (TOF) for methane formation, at different temperatures

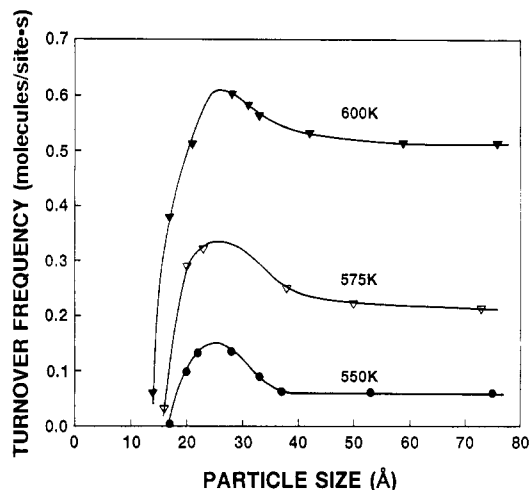


Figure 4. Ethane hydrogenolysis turnover frequencies at various temperatures (550, 575, 600 K) as a function of nickel particle size.  $P_{\text{ethane}} = 1.0$  Torr,  $P_{\text{H}_2} = 20$  Torr, and  $t = 10$  min.

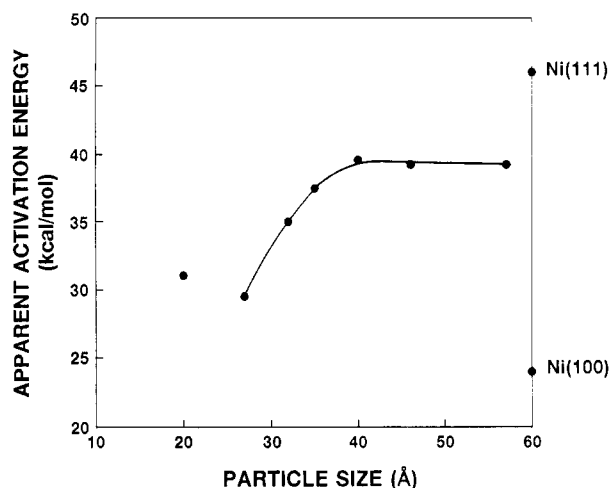
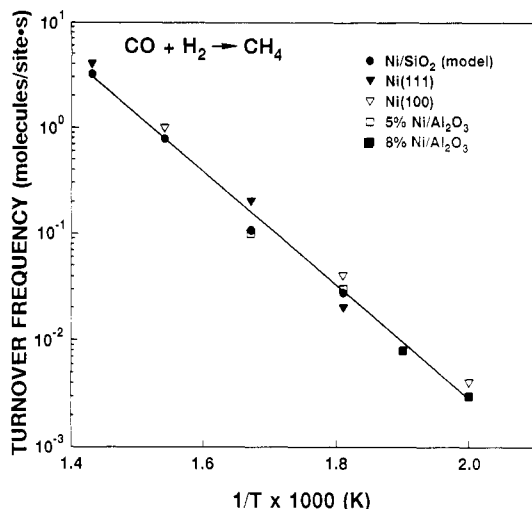


Figure 5. Activation energy for ethane hydrogenolysis as a function of particle size. Activation energies were calculated for the data of Figure 4.

(550, 575, 600 K), as a function of nickel particle size. The specific activity initially increases with particle size to a maximum at  $\sim 25$  Å. Above 25 Å, the TOF decreases to a constant value that is independent of particle size. Similar variations in TOF with particle size have been observed previously over supported nickel catalysts; the absolute activities reported here are in excellent agreement with the literature values.<sup>5,36,37</sup>

The TOF measured on a catalyst with average particle diameters of  $\sim 25$  Å also agrees well with the TOF reported for a Ni(100) single crystal. As the nickel particles increases in size, the TOF approaches the values measured over a Ni(111) single crystal.<sup>38</sup> The differences in catalytic activity of nickel (111) and (100) crystal planes are well documented with various explanations given for the origin of the higher activity on the Ni(100) surface.<sup>14</sup> For example, electronic differences, steric constraints for ethane adsorption, and preferential surface carbon formation between the two surfaces have been proposed. A clear trend of increasing rates with decreasing particle size to  $\sim 25$  Å is evident for the model Ni/SiO<sub>2</sub> catalysts.

In addition to the changes in TOF with particle size, the apparent activation energy for hydrogenolysis is found to vary. By plotting in Arrhenius form the data from Figure 4, an apparent activation energy for each respective particle size is shown in Figure 5. Initially, the activation energy decreases as the particles approach 25 Å in diameter. The lowest apparent activation energy (30 kcal/mol) for ethane hydrogenolysis on  $\sim 25$ -Å particles is similar to the reported value on Ni(100) (24 kcal/mol). The



**Figure 6.** Arrhenius plot of CO methanation over model Ni/SiO<sub>2</sub>, Ni(100), and Ni(111) single-crystal<sup>19</sup> and alumina supported Ni catalysts.<sup>15,16</sup>  $P_{\text{CO}} = 5.0$  Torr,  $P_{\text{H}_2} = 20.0$  Torr,  $T = 500$ – $650$  K, and  $t = 10$  min.

apparent activation energy increases from a low of 30 kcal/mol for the 25-Å particles to a high of ~40 kcal/mol for the relatively large particles. The apparent activation energy for the large particles approaches the value associated with a Ni(111) surface (46 kcal/mol). This change in activation energy has also been observed for supported nickel catalysts.<sup>39</sup>

**Carbon Monoxide Methanation.** CO methanation was examined with respect to the nickel particle size to demonstrate the structure insensitivity of this reaction and, accordingly, to verify our particle size characterization methods. Studies of this reaction over high surface area, supported nickel,<sup>15,16</sup> nickel single crystals,<sup>11,18,19</sup> and nickel supported on model thin-film alumina<sup>20</sup> provide extensive kinetic data for comparison. Figure 6 plots the methanation TOF in Arrhenius form of nickel (~50-Å particles) supported on a SiO<sub>2</sub> model catalyst. Included in Figure 6 are data for Ni(100) and Ni(111) single crystals<sup>19</sup> and two alumina supported catalysts.<sup>15,16</sup> The agreement in TOF among the different catalysts is exceptional and demonstrates that the model catalysts used for this study are representative of the high surface area, supported nickel catalysts. It is evident from the specific rates and activation energies (~22 kcal/mol) associated with the various nickel structures that the methanation reaction kinetics is insensitive to changes in particle morphology.

In Figure 7, a plot of the change in TOF with increasing particle size is shown. Within experimental error, the specific activity for methanation remains constant for all particles regardless of size.

The methanation TOF's reported are relative to the number of surface nickel atoms. The excellent agreement between previously reported specific rates and those observed over the Ni/SiO<sub>2</sub> model catalysts provides strong support for the procedures used to determine the number of nickel atoms at the surface. The plot of TOF versus particle size for methanation also demonstrates the reliability of the dispersion measurements. Similarities between previously reported ethane hydrogenolysis TOF's and those of the model also verify the dispersion measurements.

## Discussion

The IRAS spectra suggest that the large nickel particles consist of (100), (111), and other higher-index planes on which bridging CO adsorption is favored. The presence of (111) and (100) facets on the large particles is expected since these facets are most stable. An fcc metal, such as nickel, is purported to cluster to form cubooctahedra, composed primarily of (111) and (100) facets

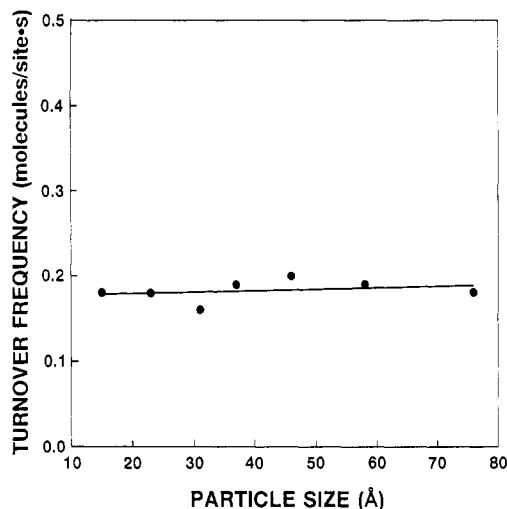


**Figure 7.** CO methanation turnover frequencies as a function of nickel particle size.  $P_{\text{CO}} = 5.0$  Torr,  $P_{\text{H}_2} = 20.0$  Torr,  $T = 600$  K, and  $t = 10$  min.

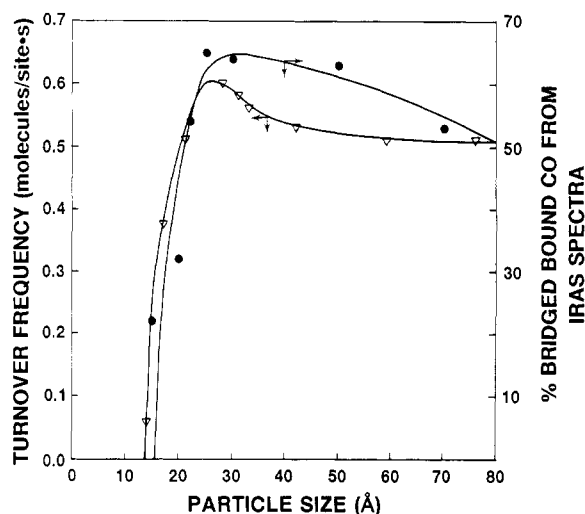


**Figure 8.** Correlation of the TOP for ethane hydrogenolysis (reaction conditions same as in Figure 4, 600 K) and the percentage of total bridge bound CO from the IRAS spectra of Figure 3.

with low-coordination edge atoms where the planes meet.<sup>40</sup> Smaller nickel particles, however, do not exhibit adsorption properties of any distinct facet. IRAS spectra indicate a major atop CO band at 2086 cm<sup>-1</sup>, a frequency much higher than that found for CO on Ni(100), Ni(110), and Ni(111) under the same conditions. This higher stretching frequency for atop CO on the small nickel particles suggests a weaker metal-CO interaction. The weaker adsorption can be attributed either to an intrinsic property of small metal clusters or to a metal-support interaction, in which transfer of electronic charge from the small metal particles to the oxide substrate takes place.

The specific reaction rate of ethane hydrogenolysis over nickel particles increases with particle size to a maximum at ~25 Å and then declines to a constant value with a further increase in size. This reactivity parallels the relative intensity change of the bridge-bound CO on the small particles. As shown in Figure 8, the percentage of bridging CO increases with particle size to a maximum at ~25 Å and then decreases. The agreement between these data indicates a similarity in the nature of bridging CO adsorption and ethane hydrogenolysis; both require at least two metal atoms. The distance between and the orientation of the surface atoms have been proposed to give rise to the kinetic differences observed for hydrogenolysis over the (111) and (100) faces of nickel. The more open Ni(100) surface exhibits a mechanism for ethane hydrogenolysis that is similar to the reaction

steps observed for CO methanation. It has been proposed that the Ni–Ni distances on the (100) surface facilitate a facile carbon–carbon bond scission for adsorbed ethane.<sup>38</sup> The resulting carbonaceous deposit is hydrogenated, and the overall apparent activation energy (24 kcal/mol) is very similar to the activation energy (25 kcal/mol) for CO methanation.<sup>15</sup>

Two factors may contribute to the activity for ethane hydrogenolysis: an intrinsic size effect for small clusters and a change of surface structure for the larger particles. The initial increase in activity (TOF) for ethane hydrogenolysis and a similar increase in the percentage of bridging CO adsorption suggest an intrinsic particle size effect. That is, the supported nickel clusters must be a certain size in order to exhibit the appropriate chemical properties. A component of this size effect may be related to a metal–support interaction. Metal clusters will interact with the oxide support, and the fraction of the total atoms contacting the support will decrease as the cluster grows. For the smallest clusters, the effect of interfacial interactions on the nature of the metal clusters could be significant. This perturbation by the support decreases quickly as the particle size increases, resulting in the plateauing of the activity.

At a sufficiently large cluster size, the effect of the silica support is negligible. However, with an increase in the particle size, the surface morphology of the metal particles changes from a relatively open to a relatively close-packed structure. For ethane hydrogenolysis this surface morphology modification explains the decrease in the TOF to a constant value and the corresponding increase in the activation energy. The hydrogenation of surface carbon ( $E_a = 25$  kcal/mol) is the rate-limiting step for the open Ni(100) surface. In contrast, for hydrogenolysis on the close-packed Ni(111) the C–C bond remains intact, and the rate-determining step ( $E_a = 46$  kcal/mol) is the breaking of the carbon–carbon bond.<sup>13</sup> The highest hydrogenolysis activity is observed for particles of  $\sim 25$  Å.

On the other hand, the rate of CO methanation does not vary with nickel particle size. This structural insensitivity is likely related to the fact that a relatively small ensemble (perhaps a single nickel atom) is sufficient to catalyze the hydrogenation of surface carbon, the critical step in the reaction sequence. It is interesting to note that the variations in the CO adsorption geometry as determined by IRAS apparently do not influence the rate of CO methanation.

## Conclusions

The facet distribution within silica-supported nickel particles changes with particle size. Large particles ( $>25$  Å) contain primarily (100) and (111) facets with minor contributions from other higher-index planes. On the other hand, smaller particles do not exhibit the spectroscopic fingerprints of specific oriented surfaces. Specific rates and activation energies for ethane hydrogenolysis and carbon monoxide methanation over the model catalysts are similar to the corresponding values found for both traditional silica-supported nickel catalysts as well as nickel single crystals. The specific activity of ethane hydrogenolysis increases with nickel particle size to a maximum value for  $\sim 25$ -Å particles and then declines. This increase in reactivity correlates with an increase in the percentage of bridging CO on the small particles,

suggesting an intrinsic particle size effect. For particles larger than  $\sim 25$  Å, the specific activity for hydrogenolysis decreases due to a higher density of close-packed facets (i.e.,  $\langle 111 \rangle$  planes) which have an intrinsic lower activity for this reaction.

**Acknowledgment.** We acknowledge with pleasure the support of this work by the Department of Energy, Office of Basic Energy Sciences, Division of Chemical Sciences.

## References and Notes

- (1) See, for example: (a) *Surface Science of Catalysis*; Dwyer, D. J., Hoffman, F. M., Eds.; American Chemical Society: Washington, DC, 1992. (b) *The Chemical Physics of Solid Surfaces and Heterogeneous Catalysis*; King, D. A., Woodruff, D. P., Eds.; Elsevier: Amsterdam, 1980–89; Vols. 1–5.
- (2) See, for example: Rodriguez, J. A.; Goodman, D. W. *Surf. Sci. Rep.* **1991**, *14*, 1.
- (3) (a) Satterfield, C. N. *Heterogeneous Catalysis in Practice*; McGraw-Hill: New York, 1980. (b) *Strong Metal-Support Interactions*; Baker, R. T. K., et al., Eds.; American Chemical Society: Washington, DC, 1986. (c) *Metal-Support Interactions in Catalysis, Sintering and Redispersion*; Stevenson, S. A., et al., Eds.; Van Nostrand Reinhold: New York, 1987.
- (4) See, for example: Vurens, G. H.; Salmeron, M.; Somorjai, G. A. *Prog. Surf. Sci.* **1989**, *32*, 333.
- (5) Carter, J. L.; Cusumano, J. A.; Sinfelt, J. H. *J. Phys. Chem.* **1966**, *70*, 2257.
- (6) Xu, X.; Goodman, D. W. *Appl. Phys. Lett.* **1992**, *61*, 1799.
- (7) Xu, X.; Goodman, D. W. *J. Phys. Chem.* **1993**, *97*, 683.
- (8) Xu, X.; Goodman, D. W. *J. Chem. Phys.* **1993**, *97*, 7711.
- (9) Xu, X.; Goodman, D. W. *Surf. Sci.* **1993**, *282*, 323.
- (10) Walkup, R. E.; Raider, S. I. *Appl. Phys. Lett.* **1988**, *53*, 888.
- (11) Goodman, D. W. *Acc. Chem. Res.* **1984**, *17*, 194.
- (12) Martin, G. A. *J. Catal.* **1979**, *60*, 452.
- (13) Goodman, D. W. *Catal. Today* **1992**, *12*, 189.
- (14) Gates, B. C.; Koningsberger, D. C. *CHEMTECH* **1992**, 300.
- (15) Vannice, M. A. *J. Catal.* **1976**, *44*, 152.
- (16) Vannice, M. A. *Catal. Rev.—Sci. Eng.* **1976**, *14*, 153.
- (17) Goodman, D. W.; Kelley, R. D.; Madey, T. E.; White, J. M. *J. Catal.* **1980**, *64*, 479.
- (18) Goodman, D. W. *J. Vac. Sci. Technol.* **1982**, *20*, 522.
- (19) Kelley, R. D.; Goodman, D. W. *Surf. Sci.* **1982**, *123*, L743.
- (20) Bischke, S. D.; Goodman, D. W.; Falconer, J. L. *Surf. Sci.* **1985**, *150*, 351.
- (21) Lueng, L. W. H.; He, J. W.; Goodman, D. W. *J. Chem. Phys.* **1990**, *93*, 8378.
- (22) Xu, X.; Goodman, D. W. *Appl. Phys. Lett.* **1992**, *61*, 774.
- (23) He, J. W.; Xu, X.; Corneille, J. S.; Goodman, D. W. *Surf. Sci.* **1992**, *279*, 119.
- (24) Xu, X.; Goodman, D. W. Unpublished.
- (25) He, J.-W.; Shea, W. L.; Jiang, X.; Goodman, D. W. *J. Vac. Sci. Technol. A* **1990**, *8*, 2435.
- (26) Conrad, H.; Ertl, G.; Kuppers, J.; Latta, E. E. *Surf. Sci.* **1976**, *57*, 475.
- (27) Campuzano, J. C.; Greenler, R. G. *Surf. Sci.* **1979**, *83*, 301.
- (28) Netzer, F. P.; Madey, T. P. *J. Chem. Phys.* **1982**, *76*, 710.
- (29) Xu, X.; Vesecky, S. M.; Goodman, D. W. *Science* **1992**, *258*, 788.
- (30) Lauterbach, J.; Wittmann, M.; Kuppers, J. *Surf. Sci.* **1992**, *279*, 287.
- (31) Berolini, J. C.; Tardy, B. *Surf. Sci.* **1981**, *102*, 131.
- (32) Marzouk, H. A.; Bradley, E. B.; Arunkumar, K. A. *Surf. Sci.* **1985**, *161*, 462.
- (33) Bertolini, J. C.; Dalmai-Imelik, G.; Rousseau, J. *Surf. Sci.* **1977**, *68*, 539.
- (34) Christman, K.; Schober, O.; Ertl, G. *J. Chem. Phys.* **1974**, *4719*.
- (35) Andersson, S. *Solid State Commun.* **1977**, *21*, 75.
- (36) Sarkany, A.; Tetenyi, P. *React. Kinet. Catal. Lett.* **1979**, *12*, 297.
- (37) Martin, G. A.; Dalmon, J. A. C. R. *Acad. Sci., Ser. C* **1978**, *286*, 127.
- (38) Goodman, D. W. *Surf. Sci.* **1982**, *123*, L679.
- (39) Yates, J. C.; Taylor, W. F.; Sinfelt, J. H. *J. Phys. Chem.* **1964**, *68*, 2962.
- (40) Van Hardeveld, R.; Hartog, F. *Surf. Sci.* **1969**, *15*, 189.